Designing Covalent Organic Framework-Based Light-Driven Microswimmers toward Therapeutic Applications

Varun Sridhar, Erdost Yildiz, Andrés Rodríguez-Camargo, Xianglong Lyu, Liang Yao, Paul Wrede, Amirreza Aghakhani, Birgul M. Akolpoglu, Filip Podjaski,* Bettina V. Lotsch,* and Metin Sitti*

While micromachines with tailored functionalities enable therapeutic applications in biological environments, their controlled motion and targeted drug delivery in biological media require sophisticated designs for practical applications. Covalent organic frameworks (COFs), a new generation of crystalline and nanoporous polymers, offer new perspectives for light-driven microswimmers in heterogeneous biological environments including intraocular fluids, thus setting the stage for biomedical applications such as retinal drug delivery. Two different types of COFs, uniformly spherical TABP-PDA-COF sub-micrometer particles and texturally nanoporous, micrometer-sized TpAzo-COF particles are described and compared as light-driven microrobots. They can be used as highly efficient visible-light-driven drug carriers in aqueous ionic and cellular media. Their absorption ranging down to red light enables phototaxis even in deeper and viscous biological media, while the organic nature of COFs ensures their biocompatibility. Their inherently porous structures with ≈2.6 and ≈3.4 nm pores, and large surface areas allow for targeted and efficient drug loading even for insoluble drugs, which can be released on demand. Additionally, indocyanine green (ICG) dye loading in the pores enables photoacoustic imaging, optical coherence tomography, and hyperthermia in operando conditions. This real-time visualization of the drug-loaded COF microswimmers enables unique insights into the action of photoactive porous drug carriers for therapeutic applications.

1. Introduction

Microrobots are tiny machines that are tailored to be controlled externally to perform individual tasks. In order to achieve external control as well as multi-purpose functionality, micro/nanobots typically require a sophisticated and specifically adapted design enabling targeted control and applications. Their primary area of use is the large field of biomedicine.[1] The microrobots should not elicit any immune response and should be compatible with the cells to enable biomedical applications.[2] Also, the propulsion method should be as noninvasive as possible, and non-toxic, excluding the use of dedicated toxic fuels.[3] For an efficient microrobot function, motion control is the first requirement, which can become more and more challenging if the liquid they are propelled in contains species that hinder propulsion or external control. Wireless motion control requires external energy input and is typically realized by magnetic or acoustic actuation,[4] but can also be realized by ultraviolet (UV)

V. Sridhar, E. Yildiz, X. Lyu, P. Wrede, A. Aghakhani, B. M. Akolpoglu, M. Sitti
Physical Intelligence Department
Max Planck Institute for Intelligent Systems
70569 Stuttgart, Germany
E-mail: sitti@is.mpg.de

A. Rodríguez-Camargo, L. Yao, F. Podjaski, B. V. Lotsch
Nanochemistry Department
Max Planck Institute for Solid State Research
70569 Stuttgart, Germany
E-mail: b.lotsch@fkf.mpg.de

A. Rodríguez-Camargo, B. V. Lotsch
Department of Chemistry
University of Stuttgart
70569 Stuttgart, Germany

P. Wrede, B. M. Akolpoglu, M. Sitti
Institute for Biomedical Engineering
ETH Zurich
8092 Zurich, Switzerland

F. Podjaski
Department of Chemistry
Imperial College London
W12 0BZ London, UK
E-mail: f.podjaski@imperial.ac.uk

B. V. Lotsch
Cluster of Excellence e-conversion
85748, Lichtenbergstrasse 4 Garching, Germany

B. V. Lotsch
Department of Chemistry
University of Munich (LMU)
81377 Munich, Germany

M. Sitti
School of Medicine and College of Engineering
Koç University
34450 Istanbul, Turkey

**ADVANCED
SCIENCE NEWS**

www.advancedsciencenews.com

**ADVANCED
MATERIALS**

www.advmat.de

or blue light, even in biological conditions, as evidenced very recently.[5] However, UV light, which is typically used for light-driven microswimmers is incompatible with biological tissues.[6] Also, visible light control, usually reported with high-intensity blue light, limits applications to transparent conditions since tissue penetration requires more red light or near-infrared light, which is a significant challenge to the field.[7]

The critical tasks of mobile microrobots are cargo uptake and delivery, often linked to biopharmaceutical classes and properties of drugs, after actively navigating to a target diseased tissue region.[8] Drug uptake and its controlled release were typically realized efficiently by encapsulation structures being a separate part of the microrobots; these were then opened in the desired conditions or where a release could be triggered otherwise. More recently, inherently porous structures, such as metal-organic frameworks[9] and porous carbon nitrides were used for such applications since their sizeable inner pore volume, reminiscent of a sponge, enables high and, even environmentally stable drug loading.[5] However, porous particle structures with many textural pores of different sizes as part of their inner surface area leave challenges for controlled loading and release from their volume.

As a last critical step to clinical applications, cell viability, the absence of foreign body reactions, and tissue biocompatibility are necessary conditions for microrobots to be used in biological contexts, which is not always easy to ensure at the same time.[2b,8a,c] For this purpose, typically biocompatible metal coatings, such as gold, titanium, or polymers are employed, but also organic-based materials are up-and-coming and were used recently without coatings, such as carbon nitrides.[5,9c,10] Compared to inorganic structures, organic materials not only offer potential biodegradability but also the high flexibility of chemical design of organic materials, especially in terms of surface functionalities and porosity, might enable more efficient and targeted biomedical applications, such as drug delivery or hyperthermia.[11] Even the most sophisticated designs with biocompatible metallic structures fail during actuation inside heterogenic biological fluids and specific-targeted drug delivery and imaging in live tissues.[12] Because of that, new materials and actuation methods should be investigated for the basic tasks for the clinical obstacles, such as intraocular motion and drug delivery.

In this work, we introduce covalent organic frameworks (COFs) as a tailorable active component to the field of micro- and nanomachines, or more precisely, light-driven microswimmers. These highly porous and crystalline materials can fulfill all the requirements listed above since their molecular structure, and also their morphology, can be designed and tuned bottom-up while enabling targeted properties.[11,13] Simultaneously, they can use visible light for photocatalytic reactions with their environment, which can also be used for active particle propulsion.[10,14] Depending on the propulsion mechanism and particle structure, the propulsion can be self-diffusiophoretic or self-electrophoretic, while allowing light-induced directional motion control via phototaxis.[15] The tailorable properties of the COF building blocks enable tuning of not only their absorption wavelength but also pore size and volume, surface polarity, and chemical affinity, which enable the loading of large and small molecule cargo based on the specific application requirements. Since such organic structures are non-magnetic per se,

unless so-called Janus or hybrid (encapsulation) structures were to be employed, the use of light is a highly promising and convenient method not only to propel them but also to trigger functions within them and to image their behavior.[15] Thanks to their promising and ion-tolerant visible-light-driven propulsion properties, we especially focus on their use in ophthalmological applications. In addition to their light-driven propulsion, their configurable particle sizes enable them to pass through the fibrillar mesh of vitreous humor ($\approx$500 nm pore size).[16] For this purpose, we select therapeutic agents and imaging modalities accordingly; then we investigate and exemplify these possibilities. We study and compare two very different modified COFs, namely TAPB-PDA-COF made from the condensation of 1,3,5-tris(4-aminophenyl)benzene and terephthaldehyde,[17] and TpAzo-COF made from 1,3,5-triformylphloroglucinol and 4,4′-azodianiline,[18] as light-driven microswimmer examples, in order to explore the microrobotic possibilities for this class of materials and to establish versatile applications. We describe their light-controlled propulsion in biological media, their biocompatibility, as well as their uptake and release of drugs that can be physisorbed to the pores of the material.[13b,19] Since these two COFs have distinct structures and morphologies, we derive design guidelines for their propulsion and cargo-related functions. For therapeutic delivery functions of microrobots, we used doxorubicin, insulin, and indocyanine green (ICG), which covers the breadth of small molecules and peptides used as therapeutic and imaging agents. We further image the motion of the COFs in real-time and potential in-vivo conditions using optical coherence tomography as well as photoacoustic imaging of COF particle swarms loaded with a near-infrared active dye (ICG). The water-soluble or insoluble drugs and the contrast agents can be loaded to track their release, allowing for first insights into the action of porous drug carriers in real-time clinical imaging modalities. In this way, we designed and investigated in detail the first organic light-controllable drug carriers for various therapeutic applications.

2. Results

2.1. COF Synthesis and Characterization

The COF structures to be used as microswimmers were selected based on their structural and optical properties and synthesized akin to a procedure reported earlier.[17,18] In brief, the TAPB-PDA-COF nanospheres were obtained by using TAPB (1,3,5-tris(4-aminophenyl)benzene) and PDA (terephthaldehyde) as building blocks, with acetonitrile and Sc(OTf)$_3$ as solvent and catalyst, respectively (see Section 5 for more details) to yield a 2D, imide linked organic network (**Figure 1**a). These 2D sheets are stacked on each together forming an ordered 3D structure with hexagonal pore channels of a diameter of $\approx$3.4 nm, as reported earlier and confirmed for the here modified synthesis by nitrogen sorption, powder X-ray diffraction (XRD), and Fourier transform infrared (FT-IR) spectroscopy analysis (Figure 1b and Figure S1, Supporting Information).[17] The obtained COF sub-micrometer particles (henceforth called nanoparticles for better discrimination) have an almost perfectly spherical shape (Figure 1c), which is beneficial for propulsion in fluids.[20] The synthesis yields a very homogeneous product with a Brunauer, Emmett, and Teller (BET)
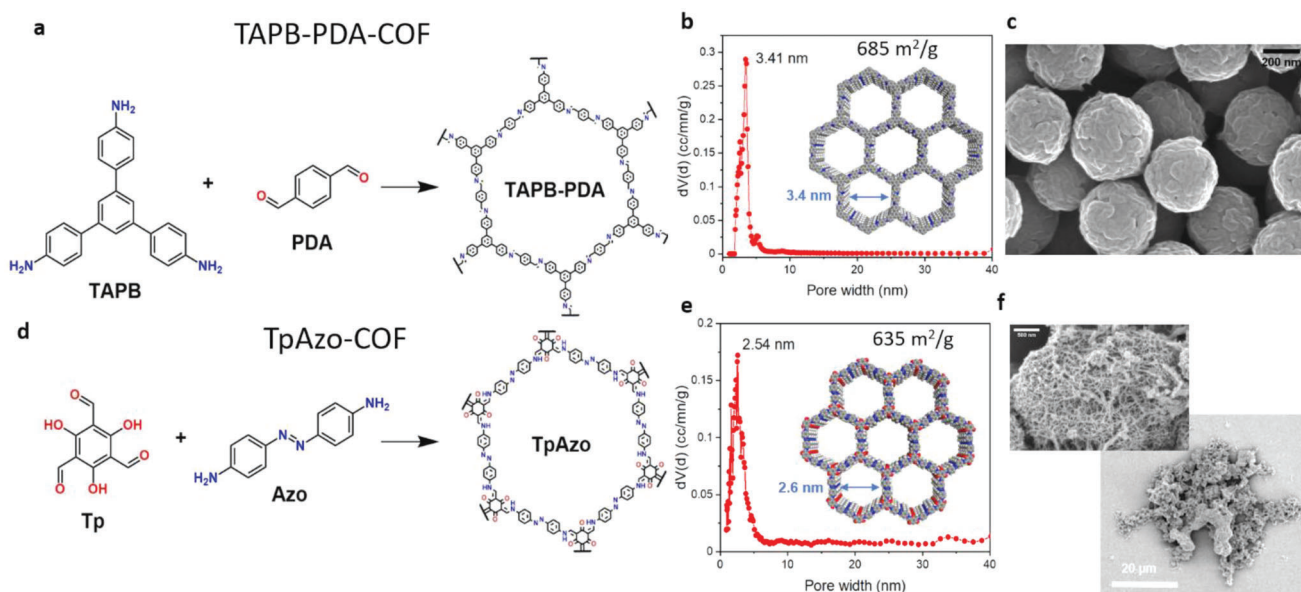
Figure 1. Structural properties of the two types of COF particles used as light-powered microswimmers. a–c) Imine-linked TABP-PDA-COF nanoparticles. a: Precursors for synthesis and molecular structure of the 2D covalent organic framework that stacks in the third dimension. b) Calculated pore size distribution from nitrogen sorption isotherms at 77 K (see Figures S1, S2, Supporting Information for details), highlighting a fairly uniform pore diameter of 3.4 nm. c) SEM image of TABP-PDA COF nanoparticles with a narrow diameter distribution (452 ± 74 nm). d-f) Azo-linked TpAzo-COF microparticles. d) Precursors for synthesis and molecular structure of the 2D network that stacks in the 3rd dimension. e) Calculated pore size distribution from nitrogen sorption isotherms at 77 K (see Figures S3–S5, Supporting Information), highlighting a relatively uniform pore diameter of 2.6 nm. f) SEM images of the TpAzo-COF microparticles with a sponge-like structure and high levels of textural porosity, including macropores and heterogeneous size distribution (7.3 ± 7.2 µm, see Figures S3–S5, Supporting Information).

surface area as high as 685 m² g⁻¹ (Figure S1c, Supporting Information) and a narrow size distribution of ≈452 ± 74 nm (Figure S2a,b, Supporting Information). TEM analysis reveals that these nanoparticles consist of agglomerated individual crystallites with sizes between 50 and 100 nm (Figure S1c, Supporting Information).

The TpAzo-COF presented here for comparison is synthesized by solvothermal condensation between 1,3,5-triformylphloroglucinol (Tp) and 4,4′-azodianiline (Azo), forming a tautomeric ketoenamine COF (Figure 1d). A highly crystalline product with a 2D molecular structure is obtained (see Figure S3, Supporting Information for structural analysis), with slightly smaller structural pores of 2.6 nm and a similar BET surface area of 635 m² g⁻¹ (Figure 1e). In contrast to the first COF, the particle morphology is much less defined, leaving open large textural voids reminiscent of a sponge (Figure 1f and Figure S4, Supporting Information). The overall particle sizes are broadly distributed (7.3 ± 7.2 µm), while being much larger. The primary crystallites forming the COF particle are only 20 nm (Figure S4d, Supporting Information), and the TpAzo-COF particles appear to be agglomerates of those.

2.2. Light-Induced Swimming in Aqueous Media

To enable light-triggered propulsion, we first investigate the light absorption properties. UV–vis spectroscopy and Kubelka–Munck analysis show that TABP-PDA-COF and TpAzo-COF have an optical band gap of 2.70 eV (**Figure 2**a and Figure S6a, Support-

ing Information) and 2.01 eV (Figure 2f and Figure S6b, Supporting Information), respectively, corresponding to 464 nm for TAPB-PDA-COF and 616 nm for TpAzo-COF, with a small absorption tail, commonly arising from defect states. Hence, visible light propulsion can be extended up to a wavelength of ≈470 nm (blue light) for the small TABP-PDA particles, and to green or even red parts of the spectrum for the large TpAzo-COF. Their light-induced propulsion was studied under a microscope in a microfluidic chamber under ambient conditions to test the phototaxis capabilities while diluting them to 10 µg mL⁻¹ typically. First, we focus on propulsion in distilled water. While in the dark, COF particles show only local Brownian motion with a mean displacement speed of 4.5 µm s⁻¹ for the TAPB-PDA and 3.7 µm s⁻¹ for the TpAzo-COF, respectively (Figure 2b,g, dashed line). When light from the photodiode is focused on the microswimmers through the microscope, their propulsion speed is significantly enhanced and becomes ballistic, as seen in Video S1, Supporting Information. The particles move toward the center of the light, then upwards. This way, the light-driven collective assembly or trapping of the microswimmers is made possible. UV excitation at 385 nm propels the TABP-PDA-COF with 13.2 ± 2.4 µm s⁻¹, while 470 nm blue light gives an even increased speed of 16.4 ± 3.1 µm s⁻¹ (≈36 bodylengths s⁻¹ (BLPS)). At 510 nm illumination, no light-enhanced swimming was observed, consistent with the absorption spectrum (Figure 2b). The Tp-Azo-COF is propelled with 4.9 ± 1.2, 12.1 ± 2.1 (≈2 BLPS), 8.2 ± 1.7, and 4.2 ± 1.2 µm s⁻¹ at 385, 470, 560, and 630 nm, respectively (Figure 2g). UV and red light hence do not increase propulsion speed significantly beyond Brownian motion, but motion becomes
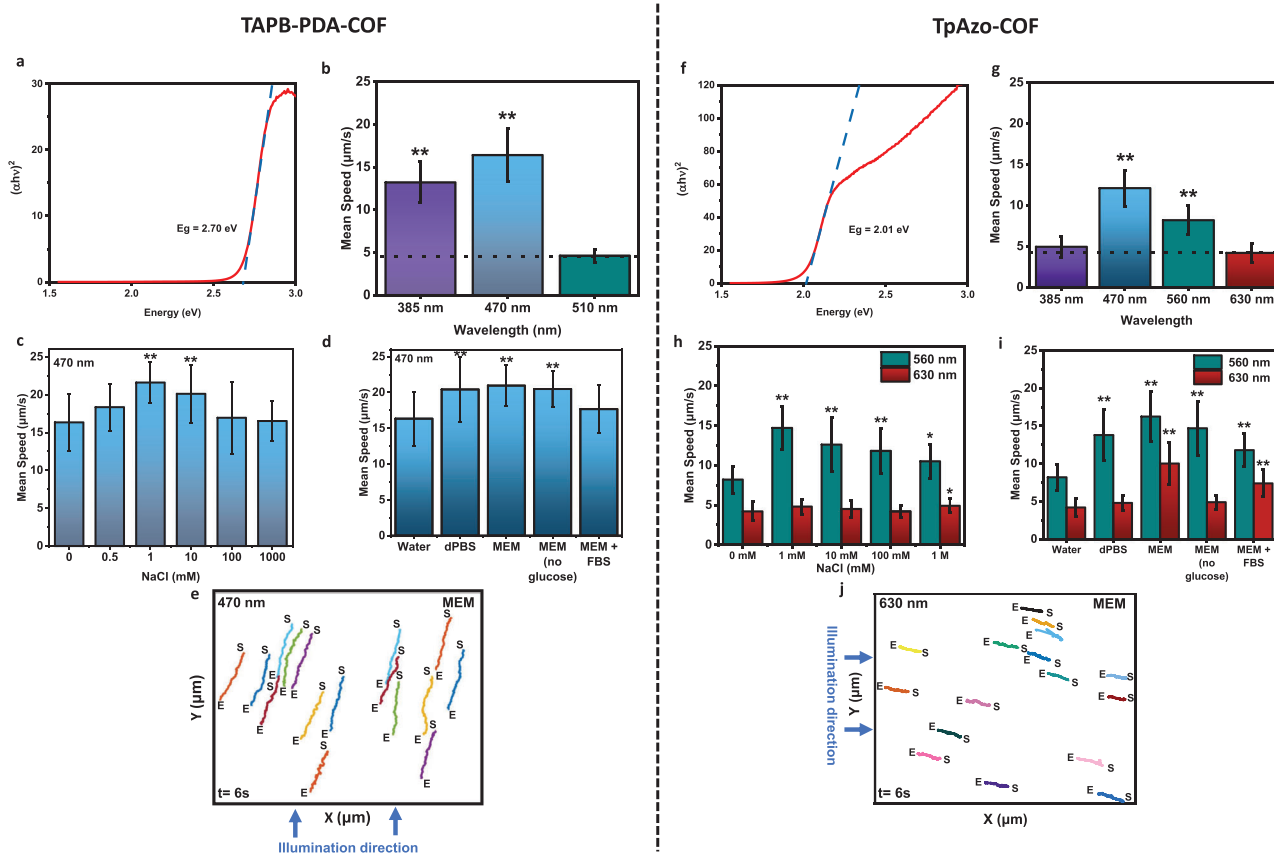
Figure 2. Optical properties and propulsion of TABP-PDA-COF and TpAzo-COF microswimmers in water and ionic media and their phototaxis behavior. a,f) Absorbance properties and optical band gap extracted from UV–vis diffuse reflectance spectra of TABP-PDA-COF (a) and TpAzo-COF (f) particles, respectively, measured in the solid state. b,g) Mean speeds of the COF microswimmers illuminated in distilled water at different wavelengths under the microscope. The dashed line denotes the local Brownian motion speed (compared to 510 nm for TABP-PDA and 630 nm for TpAzo, $*p < 0.005$, $**p < 0.001$). c,h) Propulsion in NaCl with increasing concentration and wavelength highlighting strong ionic tolerance for light-driven propulsion (compared to 0 mM NaCl, $*p < 0.005$, $**p < 0.001$). d,i) Comparison of propulsion speed in different commonly used biological media (dPBS, MEM) and MEM modified by removing glucose or adding FBS (compared to water, $*p < 0.005$, $**p < 0.001$). For (b–d) and (g–i), particle density: 10 µg mL^{-1}, $n = 50$ particles; all data presented as mean ± S.D. e,j) Phototactic control of diluted COF microswimmer particles in MEM following directional illumination from the side (S = start, E = end of trajectory) (Video S4, Supporting Information).

ballistic and thereby enables larger displacement, triggered even by green light (560 nm).

2.3. Ion Tolerance for Light-Driven Microswimmers and Phototaxis Behavior

Ionic conditions represent a major challenge for light-driven microswimmers.[21] The presence of pores, both structural and textural (=morphological), was suggested previously to enable the propulsion of microswimmers in ionic environments, which includes most of the biological fluids and cell culture media.[5] To confirm this and to widen the insights from different and better controlled structural features present in our model COFs, we first tested them in increasing concentrations of salt (NaCl), see Figure 2c,h.

When propelled at 470 nm, the TABP-PDA-COF does not decrease the speed compared to distilled water up to concentrations as large as 1000 mM. Therefore, the ionic concentration in the media at which the microswimmers' speed is halved (EI50) cannot be attributed.[22] Also, we observe a slightly increasing propulsion speed between 0.5 and 10 mM, with a maximum value of 25.2 ± 3.7 µm s^{-1} (54% increase vs distilled water, 0 mM) at 1 mM NaCl (Figure 2c). An explanation for this non-linear behavior remains to be found. Ionic environments can be influencing the Helmholtz and Debye layers, as well as the materials' inner space charge layer. As such, light-induced charge carrier stability or recombination will also be affected. Unfortunately, the experimental investigation of electrical double layers on the surface of the photoactive particles in the visible light spectrum is technically challenging.[23] On the other hand, the chlorine evolution reaction due to dissolved NaCl may be another photocatalytic pathway possibly increasing the reaction rate, and thereby the propulsion speed.[5,24] These factors currently cannot be studied or disentangled on such size and complex reaction interface. However, their propulsion speed even surpasses our previously reported PHI microswimmers, the only reported system with comparable ionic tolerance.[5]

Similarly, for the TpAzo-COFs, an increased propulsion speed compared to pure water is observed in all ionic conditions

(1–1000 mM) at 560 nm illumination, peaking also at 1 mM (14.7 ± 2.7 µm s^{-1}, 79% increase vs distilled water) and followed by a 28% relative decay to 10.5 µm s^{-1} at 1000 mM. When increasing the wavelength, no active propulsion is observed for TABP-PDA-COF (Figure 2b), but the Tp-AZO-COF exhibits slightly enhanced, ballistic propulsion even at 630 nm (4.2 µm s^{-1}) (Figure 2g).

Next, three standard biological media are studied, namely, Dulbecco's phosphate-buffered saline (dPBS), minimum essential medium (MEM), and MEM plus fetal bovine serum (FBS) (Figure 2d,i), which slightly differ in their components: dPBS contains NaCl, KCl, Na$_2$HPO$_4$, and KH$_2$PO$_4$ at ≈10 g L^{-1} (≈150 mM) in total; MEM contains the same components as dPBS and additional two amino acids, vitamins, and glucose, some of which can be redox-active agents that help extract light-generated electrons and especially holes from the microswimmers to power them.[25] FBS, slightly more viscous, adds nutrients for cell growth and imitates the conditions found within the body.[5] At 470 nm illumination, the mean speeds of the TAPB-PDA-COF microswimmers in dPBS, MEM, and MEM + FBS are 20.4 ± 4.5, 20.9 ± 2.8, and 17.6 ± 3.3 µm s^{-1}, respectively. These speeds are again higher than in distilled water (16.4 ± 3.1 µs s^{-1}). The slight decrease upon FBS addition can be attributed to the increasing viscosity or other surface interactions with the proteins present in the FBS.

Very similar behavior is observed with the TpAzo-COF at 560 nm, where the swimming speeds are equivalent to the maximum value in 1 mM NaCl, or even slightly higher (13.8 ± 3.4, 16.2± 3.4, 14.7 ± 3.6, and 11.8 ± 2.2 µm s^{-1} in dPBS, MEM (with and without glucose), and MEM + FBS). A difference however is observed when glucose, a well-oxidizable fuel, is absent—the speed is reduced.[5,25] Its vital role as fuel for propulsion is clearly visible when illuminating TpAzo at 630 nm in MEM that contains glucose, where efficient propulsion, independent of FBS, is observed (10 ± 2.7 and 7.4 ± 1.8 µm s^{-1} respectively). This purely red-light-induced photocatalytic motion in the presence of high ion concentrations and without using potent and toxic fuels is unprecedented.[15,26] However, the still efficient propulsion at 560 nm without glucose in MEM confirms that the other ingredients, including dissolved oxygen, may also assist motion induced by photocatalysis, or at least do not hamper it.[5,10] These experiments not only show the superiority in performance over current inorganic microswimmers in high-salinity media but also highlight how crucial facile redox species are that can act as fuel for propulsion, akin to photocatalysis in general, and especially if sub-band gap trap states might be partially involved (630 nm illumination).[25,27] Such a substantial shift toward the red part of the spectrum that can penetrate deeper tissues makes organic and small band gap microswimmers (especially with trap states in the optical bandgap) attractive for micromachines not just in vitro, but even for in vivo conditions.

2.4. Light-Driven Directional Propulsion Control

Phototaxis is the property by which microswimmers swim towards or away from the direction of incident light (i.e., positive or negative phototaxis), which often depends on their sur-

face charge.[28] It enables direction control, opposite to random ballistic displacement usually observed with Janus particles.[5,29] When the COF microswimmers were illuminated by a directed light source from the side with a 45° angle, both TABP-PDA-COF and TpAzo-COF microswimmers exhibited positive phototaxis and swam toward the light that can propel them (Figure 2e,j, Videos S2 and S4, Supporting Information). TABP-PDA-COF (10 µg mL^{-1}) and TpAzo-COF (10 µg mL^{-1}) particles move with mean speeds of 13.3 ± 1.8 and 7.6 ± 0.8 µm s^{-1}, at 470 and 630 nm illumination in water and MEM, respectively. This apparent increase in the particle speed compared to vertical illumination could be attributed to the larger parallel component of the light direction to the propulsion direction when the samples were illuminated from the side. When the samples are illuminated from the bottom, only the side-wise motion component is measured as a common standard, artificially decreasing the actual velocity.[29,30] Similar findings have been found on carbon nitride microswimmers, which were discussed in more detail in our previous study.[5] The required symmetry breaking is created by the side-wise illumination and, thereby, an artificially created Janus structure results from the self-shadowing of the microswimmers (Figure S9, Supporting Information).[6b,28a]

2.5. Biocompatibility of COFs

In order to be used in potential biomedical applications and to ascertain biocompatibility, microswimmers should have no significant cytotoxicity. Hence, we tested the cytotoxicity of the microswimmers with human umbilical vein endothelial cells (HUVEC) in dMEM with FBS. HUVECs are selected for biocompatibility experiments because of their common usage in retinal co-culture models to mimic retinal vasculature.[31] Different concentrations of TAPB-PDA-COF and TpAzo-COF microswimmers (3.1–25 µg mL^{-1}) were incubated with HUVECs in the dark, and their viability was investigated with calcein-based live/dead fluorescence staining of the cells after 24 h. The cells with TABP-PDA COF were completely viable, and they did not show any significant decrease in viability even at high concentrations, both with illumination and without illumination at 470 nm with maximum light intensity, 387 mW cm^{-2}, for 30 min), as seen in **Figure 3**a, which is visible also in live cell fluorescent images in Figure 3b. TpAzo-COF (Figure 3c,d) shows lower cell viability in comparison with TAPB-PDA-COF, with 93% and 75% HUVEC cell viability in 25 µg mL^{-1} concentration (in dark and with 630 nm illumination (117 mW cm^{-2}, for 30 min), respectively. Also, at concentrations of 3.1 µg mL^{-1}, the viability is decreased to 88% in comparison to the TABP-PDA COF. However, this fairly good viability indicates that also the TpAZo COF can be used at lower concentrations for drug delivery applications. Generally, illumination seems not to affect the viability at low concentrations (3.1 and 6.25 µg mL^{-1}), and only slightly at 12.5 and 25 µg mL^{-1} for both COFs. These results also suggest that light-induced propulsion induces only minimal cytotoxicity in the range of light-driven propulsion periods. Compared to carbon nitride microswimmers, which have a larger band gap (2.7 eV, 450 nm) and a very low-lying valence band, and therefore enable more redox reactions with organic matter, including cells in principle, the use of 470 or 630 nm
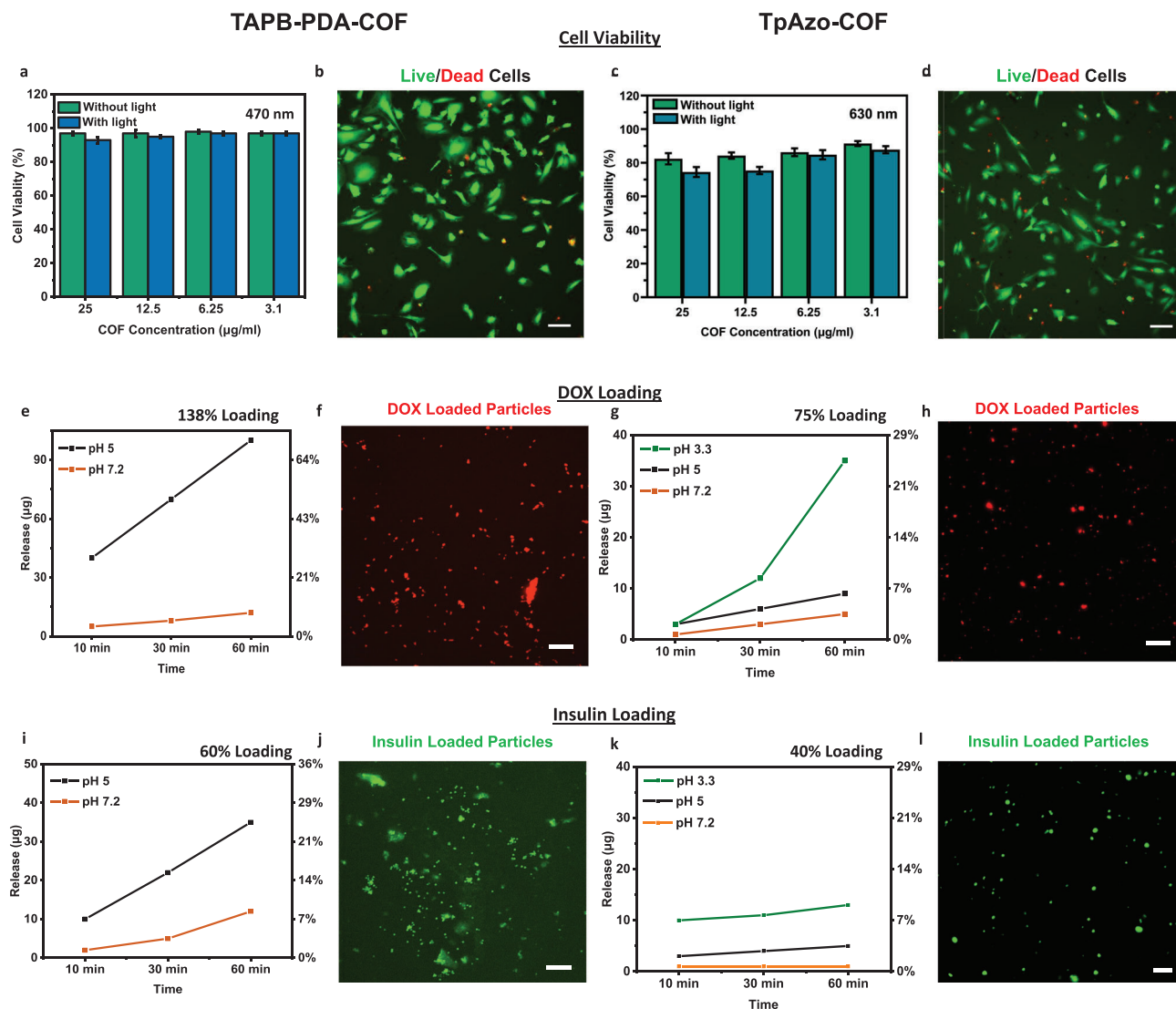
Figure 3. COF microswimmer biocompatibility, drug loading, and triggered release properties. a–d) In vitro cell viability results for COF microswimmers a,c) cell viability percentages of HUVEC cells in the presence of increasing TAPB-PDA-COF and TpAzo-COF microswimmer concentrations with/without 470 and 630 nm illumination, respectively, for 30 min, mean ± S.D. b,d) Corresponding fluorescence images of live cells (green) and dead cells (red) with 25 µg mL^{-1}, 30 min, 470 and 630 nm, respectively. e–h) DOX uptake and release results for COF microswimmers. e) TAPB-PDA-COF loading and release capacity with Doxorubicin (DOX) in MEM at different pH over time, reaching 138% for TABP-PDA-COF loaded in MEM. f) Corresponding fluorescence image of DOX (red) loaded TAPB-PDA-COFs at 25 µg mL^{-1} concentration. g) TpAzo-COF with 75% loading and their subsequent stepwise release at different pH conditions; in neutral pH (7.2), slightly acidic conditions (pH = 5), and acidic (3.3) as encountered around cancer cells. h) Corresponding fluorescence image of DOX (red) loaded TpAzo-COFs at 25 µg mL^{-1} concentration. i–l) Insulin uptake and release results for COF microswimmers. i) Insulin loading of TAPB-PDA-COF with 60% loading in MEM and release in different pH values over time. j) Corresponding fluorescence images of FITC (green) labeled insulin-loaded TAPB-PDA COFs. k) Insulin loading of TpAzo-COF with 40% loading in MEM and its release at different pH values over time. l) Corresponding fluorescence images of FITC (green) labeled insulin-loaded TpAzo-COFs. All scale bars are 100 µm.

light with our TABP-PDA COFs and TpAzo COFs shows potential for reduced cell death (with 97% and 88% cell viability after 30 min of light in 3.1 µg mL^{-1} concentrations of TAPB-PDA-COFs and TpAzo-COFs, respectively) and makes especially the TABP-PDA COFs more applicable to practical applications such as drug delivery.[32] A previous study with primary cells from mouse splenocytes further confirmed no detectable level of IL-12 (a pro-inflammatory cytokine) in the untreated samples in concentrations used above in the dark.[33]

2.6. Drug Loading, Drug Delivery, and Hyperthermia

To explore the COF microswimmer's applicability to biological environments, we also studied their potential as drug carriers with different pharmacological agents. The differently pronounced textural and structural porosity of the TABP-PDA and TpAzo-COFs (see Figure 1 and Figures S1–S4, Supporting Information), which enables ionic tolerance (Figure 2c,h), is not only beneficial for motion but also as space to take up,

transport and deliver therapeutic drugs. We studied and compared how the structural features enable interactions with such cargo in the following experiments. For this reason, we chose an imaging agent, indocyanine green (ICG), and two different pharmacological agents with different Biopharmaceutics Classification System (BCS) classes: doxorubicin (DOX) (Class III) and insulin (Class I).[34] Also, both pharmacological agents are currently used to treat common ocular disorders.[35]

First, we tested the loading of DOX, a chemotherapeutic agent against various cancer types, including retinoblastoma.[36] 200 µg of DOX was added to a suspension of 100 µg of COF microswimmers dispersed in 1 mL MEM, resulting in 138 µg DOX encapsulated (loading efficiency of 138%) on the TABP-PDA-COF microswimmers after 24 h, and 75% for TpAzo-COF. Due to the small molecular size of DOX ($\approx$1.1 nm approximate molecular diameter[37]), the molecule should fit into the structural pores of both COF structures (3.4 and 2.6 nm), while adsorbing also on the inner textural surface. Since the overall surface areas are similar within 10%, it appears that differences in polarity or hydrogen bonding, possibly mediated by the carbonyl groups of TpAzo-COF, enable electrostatic repulsions with the DOX molecules and interfere with DOX uptake in TpAzo-COF structures, which is also correlated with the zeta potential measurements. While the positive zeta potential of the TABP-PDA-COF ($\zeta_{\text{TABP-PDA-COF}} = 12.13 \pm 1.28$ mV) reduces agglomeration and enables sufficient drug loading values, the negative zeta potential of the TpAzo-COF ($\zeta_{\text{TpAzo-COF}} = -19.67 \pm 0.68$ mV) reduces drug loading due to electrostatic repulsions.[38] In addition, a lower crystallinity and thereby, possibly decreased accessible pore volume of TpAzo-COF are expected to lead to reduced DOX uptake. Overall, the DOX uptake of both COF materials is among the highest reported, also relative to other artificial structures using physical encapsulation.[5,39]

The DOX release can be achieved by changing the pH to slightly more acidic conditions, that is, from pH = 7.2 to 5.5 (Figure 3e,g), which is achieved by adding HCl to PBS. The TABP-PDA microswimmers cumulative release 95 µg of DOX within 60 min, which is significantly boosted compared to the weak, passive release also observed (12 µg). The passive release is commonly observed when drugs such as DOX are not entirely trapped or encapsulated within porous structures but physisorbed to the surface. Encapsulation within the TpAzo-COF, with a more open texture, appears more stable, as evidenced by the lower passive release at pH 7.2 (5 µg in 60 min). In line, a reduction of pH to 5 only releases 7% in 60 min, whereas a pH 3.5 yields 25% and is more reasonable as a cumulative release trigger. The acid-triggered DOX release in the TABP-PDA-COF and TpAzo-COF microswimmers can be visualized in fluorescence imaging in Figures 3f, and 3h, respectively. The enhanced drug delivery of microswimmers at lower pH has the potential to enable targeted therapy in tumor or infection environments, which typically have more acidic pHs.[40]

We also studied the loading and release of peptide (insulin), a frequently used drug in diabetic retinopathy and convenient for light-controlled drug release applications.[41] Its larger molecular size of $\approx$3 nm makes larger pore sizes on the COFs desirable to allow for an efficiently encapsulated loading. Indeed, insulin loading was observed on both COFS, 60% for TABP-PDA-COF (3.5 nm pore size) and 40% for TpAzo-COF (2.6 nm pore size)

(Figure 3i,k), which suggests that physisorption of the drugs occurs on the outer surface of the textural pores and that the structural pores can assist stable uptake.

Similar to DOX release from the COF structures, changing pH enables insulin release from both COFs. While the TABP-PDA-COF shows a continuously increasing cumulative release of $\approx$35 µg mL^{-1} within 60 min at pH 5 already, which may be desirable for slower dosing, the TpAzo-COF releases its cargo rather instantly (within 10 min), and at lower amounts ($\approx$10 µg mL^{-1} in more acidic pH 3.3 again). With both drugs, no visible light-triggered release was observed, opposite to the carbon nitride systems reported earlier with DOX. However, as seen herein, the absence of such a property can be very beneficial since it enables the decoupling of motion control and drug release, which would otherwise have to co-occur.[5]

As an imaging agent to load onto COFs, we used ICG dye, commonly used in diagnosing retinal diseases.[42] First, we investigated ICG loading and near-infrared laser-induced hyperthermia capabilities; then, we focused on medical imaging of ICG-loaded COF microswimmers with photoacoustic imaging and optical coherence tomography. As is the case with drug delivery, TABP-PDA-COF has a pore size larger than the size of the ICG ($\approx$2.9 nm molecular diameter on its longest axis); hence, the drug is presumably loaded better into the structural pores of the TABP-PDA COF (3.5 nm), while in the case of TpAzo-COF, it appears to dominantly bond to the bigger, textural pores (**Figure 4**a). After ICG was loaded onto both TpAzo-COF and TAPB-PDA-COF microswimmers at two different loading levels (50% and 100%, w/w), they were irradiated with a near-infrared (NIR) laser at 808 nm.[43] ICG-loaded TABP-PDA-COFs achieved quick and strong heating to 66 and 69 °C after only 3 min of 808 nm NIR irradiation for 50% and 100% loading, respectively. Compared to TABP-PDA-COFs, ICG-loaded TpAzo-COFs heated up to 42 and 45 °C for 50% and 100% loading under the same NIR illumination conditions (Figure 4b,c). Heat generation and accumulation are always affected by heat transport to the environment. Assuming similar absorption and hence heat generation at the same loadings, these findings indicate that indeed, ICG transfers the heat slightly better by dense binding to TABP-PDA COF and that the TpAzo COF dissipates accumulated heat faster to the environment due to its more open shape, and thereby reaches lower temperatures over extended times. In both cases, this NIR-controlled hyperthermia behavior of both COFs could be helpful for novel intraocular photodynamic therapy application, which is already in the clinical trial phase for ICG dye.[42] Compared to other novel intraocular photothermal therapy agents in the recent literature, especially TABP-PDA-COFs with pores enabling ICG uptake into the material's structural pores and intense heating from 25 to 69 °C in 3 min, show significantly better heating rate for the photodynamic combined therapy applications that are used to degrade cells by heat generation.[44]

2.7. Photoacoustic Imaging and Optical Coherence Tomography

Imaging microswimmers as they move in different fluids is one of the most critical enablers for their potential in vivo applications.[45] For this purpose, we selected to study two clinical imaging methods: optical coherence tomography (OCT)
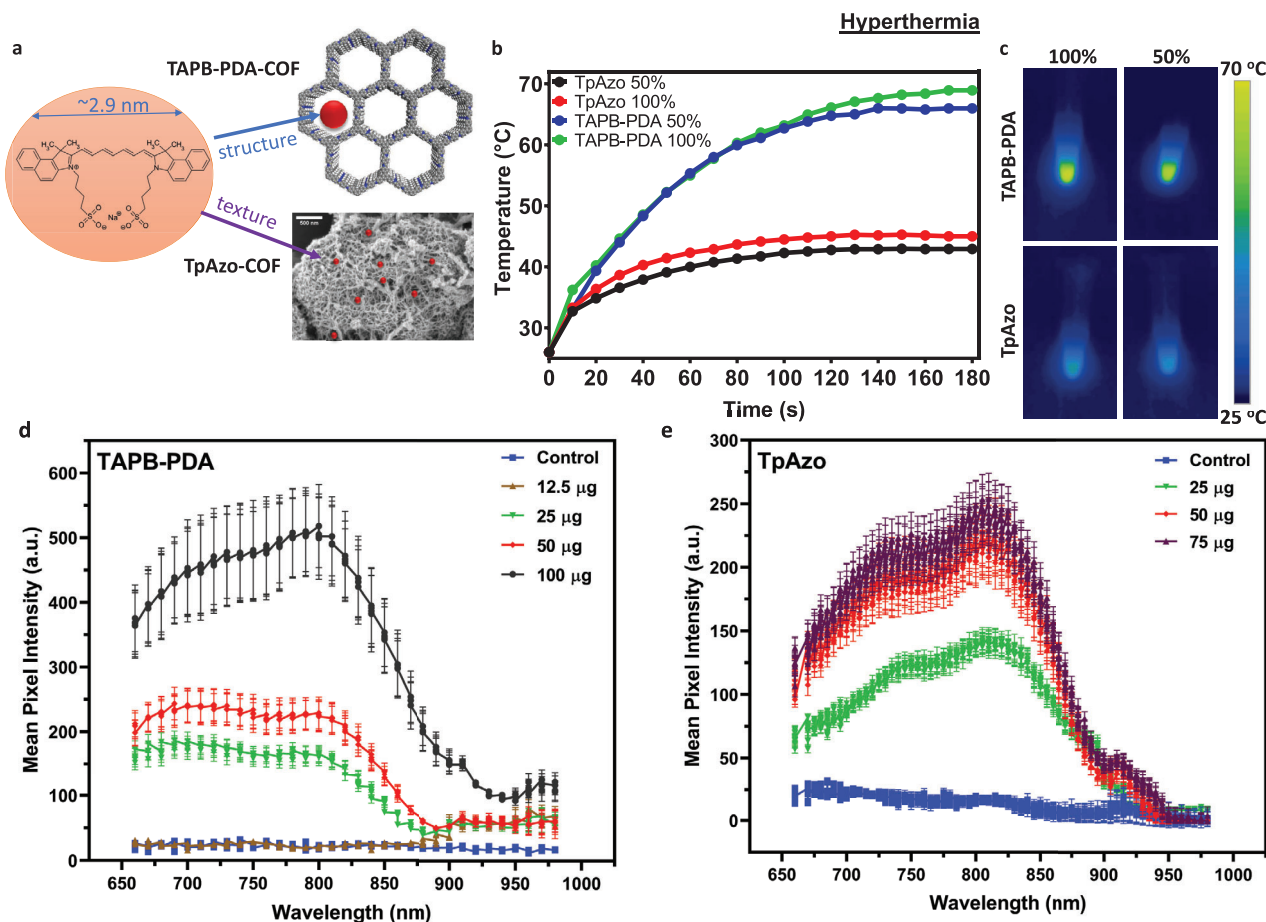
Figure 4. Indocyanine green (ICG) loading, imaging, and hyperthermia functions of both COF microswimmer types. a) ICG uptake into suitable structural pores (TAPB-PDA-COF) or texturally porous structures (Tp-Azo-COF). b,c) NIR-based heating of 50% and 100% ICG-loaded COF particles. d) Intensity of photoacoustic signal versus ICG loading, highlighting high sensitivity regimes at low loading concentrations for TAPB-PDA-COF microswimmers. e) The photoacoustic signal intensity versus ICG loading highlights high sensitivity regimes at low loading concentrations for TpAzo COF microswimmers.

and photoacoustic (PA) imaging. OCT is the gold standard high-resolution clinical imaging method to observe intraocular structures and is accessible in most ophthalmology clinics worldwide.[46] PA is an emerging imaging technique that combines the resolution of optical imaging with the depth of penetration of ultrasound imaging. In recent years, PA has been used in ophthalmology as it shows significant advantages in imaging deep ocular structures, such as lymphatic drainage and choroidal vasculature.[47] While in the PA imaging method, ICG was used as a contrast agent to enhance the visualization of COF microswimmers in the complex environment of intraocular fluids, COFs were imaged in intraocular structures and ocular fluids without any contrast agent during OCT imaging. Different concentrations of ICG are loaded onto the COF microswimmers and imaged (Figure 4d,e). While TAPB-PDA-COFs achieve up to 500 mean pixel intensity (MPI) at 815 nm, which is the highest peak in the emission spectrum of ICG, TpAzo-COFs achieve 250 MPI under the same imaging conditions. These signal intensity increases correlate with the concentration of the ICG in the COF loading suspension and also the drug uptake ability of both COFs, which correlate with other drug loading experiments. Imaging

uptake and delivery of therapeutic agents on microswimmers will be helpful in the targeted in vivo drug delivery experiments.[48]

Next, the light-driven propulsion of the COF microswimmers in intraocular fluids was observed using PA imaging. In both vitreous and aqueous fluids, COFs were illuminated in the same fashion as in the light-induced swimming experiments in various media and then tracked with photoacoustic imaging for 30 min (**Figure 5**a–c). Except for TpAzo-COF in vitreous humor under 630 nm light illumination, an increased ICG emission signal was observed in the focus areas for all COF-injected fluids compared to areas without light illumination. These results highlight that the light-driven collective motion of both COF microswimmer types is trackable under PA imaging, which is the first photoacoustic imaging application for organic microswimmers.

For clinical applicability, we observed and measured the light-driven swimming of COF microswimmers in intraocular fluids under real-time OCT. While the mean speeds of the smaller and spherical TAPB-PDA-COFs were 12.1 ± 1.7 µm s^{-1} in aqueous humor and 7.6 ± 0.8 µm s^{-1} ($\approx$16.8 BLPS) in the vitreous humor, mean speeds of TpAzo-COFs were slightly increased to 14.2 ± 1.5 µm s^{-1} in aqueous humor and 8.8 ± 1.0 µm s^{-1} ($\approx$1.25

**ADVANCED
SCIENCE NEWS**

www.advancedsciencenews.com
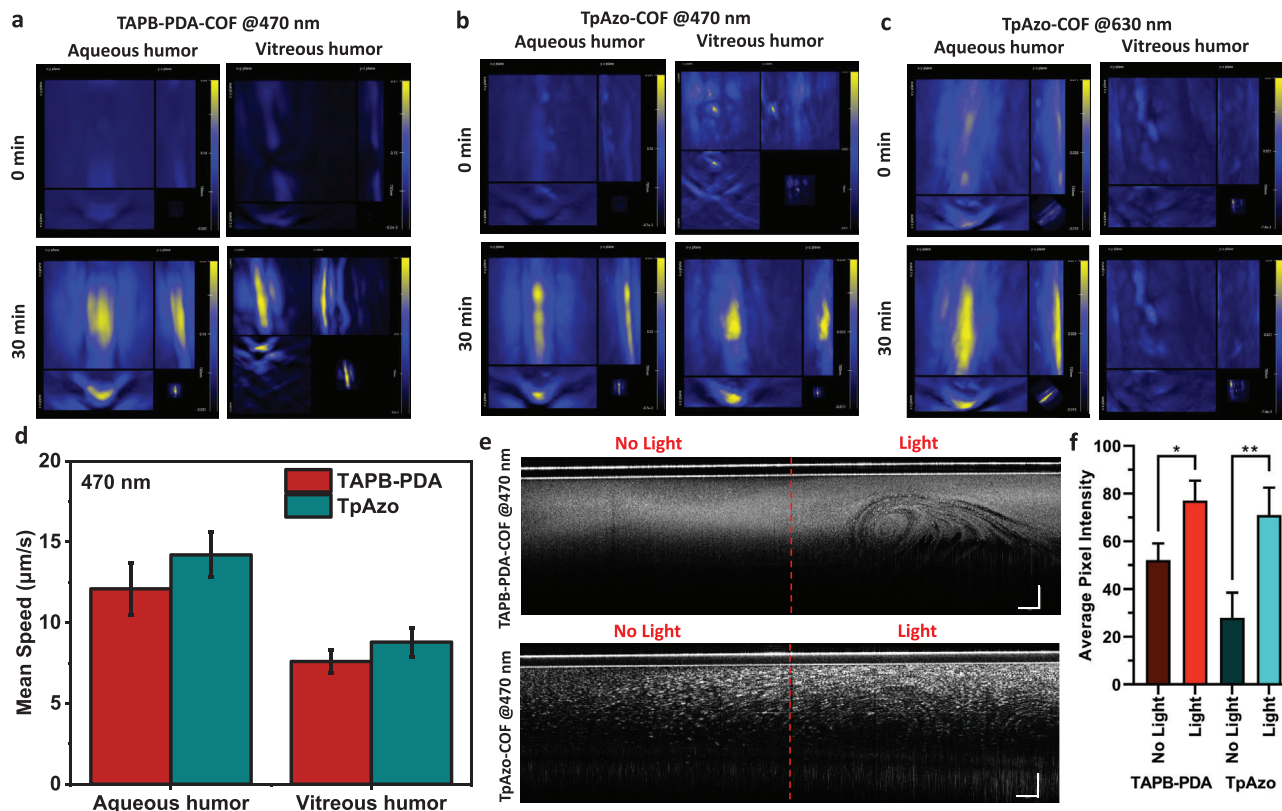
**ADVANCED
MATERIALS**

www.advmat.de

Figure 5. Real-time imaging of COF motion by photoacoustic and optical coherence tomography imaging modalities. a–c) Photoacoustic imaging of focused light-driven actuation of ICG-loaded COFs in both intraocular fluids. After 30 min, the accumulation of COF microswimmers in the focus of the light with different wavelengths is visible. d) Mean speeds of COF microswimmer particles illuminated with 470 nm light in intraocular fluids (Video S3, Supporting Information). e) Optical coherence tomography images of COFs in aqueous humor (Video S5, Supporting Information). The COF swimmers' light-driven movement on the tubing's light-applied side is visible. The scale bar is 500 µm on each axis. f) Comparison of the average pixel intensity with or without light application for both COF microswimmers in aqueous humor after 10 min of light application. Both COF microswimmers accumulated in the illuminated areas of the tubings ($n = 6$, *$p < 0.005$, **$p < 0.001$).

BLPS) in the vitreous humor under 470 nm light illumination (Figure 5d and Video S3, Supporting Information). Compared to the previous intraocular microrobotic studies employing magnetic actuation of helical microswimmers, the speed of the microswimmers in terms of BLPS was significantly higher, ≈16.8 BLPS in the current study versus ≈5.3 BLPS for the fastest magnetic intraocular microswimmers previously.[12c] Light-driven accumulation behavior of both COF microswimmer types in the focus of the light was trackable under real-time OCT imaging without any contrast agent loading (Figure 5e and Video S5, Supporting Information). Even after 10 min of light application, due to the light-driven aggregation of the microswimmers in the light-applied areas, average pixel intensities were significantly increased (52.1 ± 7.0 in the dark, 77.1 ± 8.4 in light for TAPB-PDA-COFs and 27.9 ± 10.6 in the dark, 70.9 ± 11.6 in light for TpAzo-COFs) (see Figure 5f). Additionally, their light-driven propulsion in 470 nm wavelength light was also trackable even inside an ex vivo porcine eye with anterior segment OCT imaging (Video S6, Supporting Information). These findings in OCT imaging experiments of the COF-based microswimmers indicate that they could solve the drug diffusion challenges in intraocular therapies.[49] The COF-based microswimmers are the first intraocular microswimmers that can be propelled and trackable

inside the eye without any contrast agent or surface modification. TpAzo-COFs were actuated faster, opposite to the previous experiments, which highlights that a perfectly spherical shape of TAPB-PDA-COFs alone is not of dominating benefit for mesh-like heterogeneous structures. Although the reasons for this inverted swimming speed remain to be clarified and likely depend on photocatalytic reaction rates in the respective environment, it is possibly also linked to the increased viscosity and fibrillary mesh structures in the aqueous and vitreous humor that overall decrease the propulsion speed of both COF microswimmer types compared with previous aqueous conditions.[16] These results show that both COF microswimmer types are suitable microrobotic drug delivery agents under both PA and OCT imaging while enabling actual biomedical applications inside body fluids, especially for intraocular structures. With the help of their promising drug delivery and NIR-based hyperthermia abilities, they could solve the active retinal drug delivery problems in various ocular disorders.[35] They could be easily loaded with DOX for chemotherapy without adverse effects on retinoblastoma patients or with insulin to treat increased ocular pressure.[50] While magnetic microswimmers have limitations due to the magnetic actuation systems, which require electromagnetic coils around the patient or target organ that can be complex and inflexible,

**ADVANCED
SCIENCE NEWS**

www.advancedsciencenews.com

**ADVANCED
MATERIALS**

www.advmat.de

visible light-driven COF-microswimmers can be used without these limitations, making them a more viable option for minimally invasive medical procedures.[12b,c]

3. Discussion

In this paper, two structurally and texturally distinct COF microswimmer types with different nanopore sizes were investigated for potential drug delivery applications as organic multifunctional micromachines. Using different building blocks, we synthesized two distinct COF microswimmers with different pore sizes and surface areas (Figure 1). Thanks to the tunability of COFs, pore sizes of the COF-based structures can range from ≈1.8 to 10 nm;[51] and surface areas can achieve more than 3300 m^2 g^{-1}.[52] In addition to pore size tunability, modifications of the ionic groups on the surface of the COFs will change their hydrophilicity and thus, their drug-loading capacities. Comparison of the COFs with two distinct morphologies and drug loading capabilities yielded promising results in terms of biocompatibility, imaging, drug delivery, and visible light-induced propulsion in ionic and biological media, surpassing the applicability of current magnetically actuated microswimmer-based systems—without a need of further structural modification or sophisticated structural engineering. Simultaneously, the COF microswimmers can be propelled by the almost full spectrum of visible light in ionic and biological conditions (Figure 2). Compared to TABP-PDA-COF, TpAzo-COF was actuated by a larger wavelength range including green light, which is rationalized by a bathochromic shift induced by the azo groups and donor-acceptor interactions.[53] In a recent study, Yang et al. achieved high speeds (≈120 BLPS at max. speed) with near-infrared light-driven microrobots in deionized water.[54] Unfortunately, due to high light intensities for actuation (0.6–1.2 W cm^{-2}), higher than the maximal permissible exposure limits, and larger microrobot body size than the average pore size of the hyaluronic acid mesh, these swimmers are not feasible for biomedical application.[16,55] Thanks to the tunability and modifiability of COFs with different linkers and linkages, COF-based microswimmers could outperform hydrogel-based microrobots in the near future.

Although some medium-dependent propulsion trends at low salt concentrations remain to be clarified, their porous structure, coupled with photocatalytic activity, seems key to efficient photocatalytic motion without dedicated toxic fuels or harm to the tissue. A compact spherical shape, as achieved by the size-modified synthesis of the TABP-PDA-COFs, appears beneficial for fast propulsion, enabling bubble-free motion at 36 BLPS while opening up possibilities for mobility in the intraocular region. On the other hand, large, and texturally more porous structures, as observed for the TpAZo-COF, enable similar absolute propulsion speeds in ionic conditions, albeit at a much-reduced speed relative to their size (≈2 BLPS). The explanation for this behavior remains to be found and rationalized by numerical models, especially since simple fluid dynamics and the applicability of Reynolds numbers, which do not include inner flow, appear not to be suited for these systems.[56] Both microswimmers allow for precise motion control as single particles by their phototactic properties, enabling phototaxis and photo-trapping in various ionic media for microparticle actuation in principle (Figure 2).[5,10,26] While controlled photocatalytic propulsion origi-

nates from symmetry breaking that is induced by collimated illumination, shining light on one hemisphere and leading to shadowing of the other hemisphere, the underlying chemical mechanisms of the propulsion cannot be easily identified due to the complexity of the biological media and its possible redox reactions, as well as mobile particle interactions (Figure S9, Supporting Information).[56]

We show that large structural and textural pores enable the loading of different drugs and dyes, but that the pore size itself is not the sole descriptor for stable uptake, since textural surface area also contributes to drug binding. This is clearly visible by the different uptake behaviors of the small drug DOX (Figure 3), whereas larger molecules, such as insulin or ICG, can stay more stably bound, even in lower loading amounts (Figure 4). The physical encapsulation and pH-dependent release of the active pharmacological agents from the COF-based structures due to the increased porosity have been demonstrated in previous studies.[57] Since the drug binding and release mechanisms are also affected by chemical interactions between the COF backbone and the drug, irrespective of pore size and surface area, future material design should focus on optimizing these interaction factors to broaden our insights further.

The versatility of COFs, not only on the morphological but especially on a molecular level, is anticipated to enable tailored approaches to tune the adsorption and desorption properties of drugs, akin to their use on gas sorption.[13a,58] Modifications of these interactions, especially by external stimuli, such as pH changes, light, viscosity changes, and oxygen content, can enable the desired interaction strength with the cargo and its release kinetics. Our previous work on optoionic carbon nitrides (CN$_x$) paved the way for the use of porous materials for light-driven, photocatalytic propulsion in aqueous media containing ions.[5] However, CN$_x$ are inflexible, allowing no modification of the molecular backbone, porosity, or optical band gap. In contrast, COFs can be designed bottom-up, enabling customization of the band gap, structural pores, and surface area.[59] COFs can also absorb red light, making them valuable in biomedical applications for drug encapsulation and release.[60] COFs offer broader possibilities in light-driven microrobotics and drug delivery, including therapeutic agents and diagnostic dyes, as well as NIR heating-based photothermal therapy.

In addition to the drug delivery capabilities, COFs with ICG loadings enable their high-contrast PA and OCT imaging inside the organs. In principle, both of them enable the visualization of swarms and motion of large individual particles, providing more detailed insights into local propulsion and release properties inside the eye or soft tissues where visible light cannot easily penetrate since the ICG loading can be kept very low in the porous COFs while maintaining a high signal intensity (Figure 4). Thanks to the COFs' drug loading capabilities, optical coherence tomography inside eye tissue also enables real-time imaging studies of drug-loaded microswimmers and evaluation in intraocular fluids and structures, laying the grounds for a more detailed understanding of release properties and burst kinetics for various therapeutic agents. These medical imaging and controllable drug release possibilities are anticipated to enable tailored, targeted, and especially semi-autonomous therapy not only for in vitro but also for in vivo applications.[61] In the near future, COF structures could be improved with other properties, such

**ADVANCED
SCIENCE NEWS**

www.advancedsciencenews.com

**ADVANCED
MATERIALS**

www.advmat.de

as biodegradability, for biomedical applications by multiplexing COFs with other fabrication methods.

4. Conclusion

We have studied two structurally and texturally distinct COF microswimmer types with different nanopore sizes toward their potential intraocular medical applications as multifunctional organic microswimmers. By decoupling the COF microswimmer motion control and hyperthermia mechanism via different light wavelengths, a broad range of independent functionalities is made possible on these porous organic structures in parallel. In addition to that, the pH-dependent drug release mechanism of COF swimmers increases their multifunctionality in clinical settings. We anticipate that simultaneous imaging, drug release, and NIR light-assisted photothermal therapy capabilities will offer additional therapeutic avenues compared to current state-of-art noninvasive photodynamic therapy techniques,[62] thus boding well for multimodal therapy and imaging of retinal diseases, such as retinoblastoma, diabetic retinopathy, or glaucoma.

5. Experimental Section

Synthesis and Preparation of Covalent Organic Frameworks: Synthesis of TAPB-PDA-COF was carried out according to a previous report with minor changes.[17] In a typical colloidal reaction, 1,3,5-tris(4-aminophenyl)benzene (TAPB) (0.030 mmol, 10.4 mg) and terephthaldehyde (PDA) (0.044 mmol, 5.96 mg) were dissolved in 14 mL acetonitrile. After 10 min of sonication, a solution of $Sc(OTf)_3$ (0.014 mmol, 7.00 mg) in 7 mL acetonitrile was added dropwise at room temperature under slight stirring. After 24 h of reaction, the solvent was exchanged for distilled water by centrifugation for five times ($795 \times g$ for 10 min each). For solids characterization, the particles were precipitated by adding 0.5 mL of 1 M NaCl solution, washed with methanol, and dried by supercritical CO_2 on a Leica EM CPD300 instrument. TpAzo-COF was synthesized according to a previous report.[63]

Brunauer–Emmett–Teller Measurements and Analysis: Nitrogen sorption measurements were performed on a Quantachrome Instruments Autosorb iQ MP at 77 K. Before the gas adsorption studies, the samples were degassed for 12 h at 120 °C under a vacuum. Multipoint BET surface area calculations and pressure ranges were chosen according to the linear region on the BET plot in the range between 0.05 and 0.35 P/P_0. Pore size distribution was determined from Nitrogen adsorption isotherms using the NLDFT cylindrical pores in the carbon model for nitrogen at 77 K.

PXRD Measurements and Analysis: Powder X-ray diffraction experiments were performed on a Stoe Stadi P diffractometer (Cu-$K_{\alpha 1}$, Ge(111) in Debye–Scherrer geometry. The samples were measured in sealed glass capillaries (OD = 1.0 mm) and spun for improved particle statistics.

Transmission Electron Microscopy and Scanning Electron Microscopy: Transmission electron microscopy was performed with a Philips CM30 ST (300 kV, LaB_6 cathode). The samples were prepared dry onto a copper lacey carbon grid (Plano). Images were recorded with a TVIPS TemCam-F216 CMOS camera. The program EM-Menu 4.0 Extended was used for analysis.

SEM images were obtained on a Zeiss Merlin or a VEGA TS 5130 MM (TESCAN) with an InLens detector using electron energy of 1.5 kV. The samples were cast on indium-doped tin oxide (ITO) substrates, and a 3 nm-thick iridium film was sputtered on them to reduce charging.

UV–vis Measurements and Analysis: For diffuse reflectance UV–visible absorption, spectra were collected on a Cary 5000 spectrometer (referenced to barium sulfate). Absorption spectra were calculated from the reflectance data using the Kubelka–Munk and assuming a direct band gap.[64]

Zeta Potential Measurements: The zeta potential was determined using a Malvern nano Zs zetasizer. Dispersions of 0.5 mg mL^{-1} COF in 10 mM aqueous NaCl were sonicated 15 min before zeta potential experiments. Surface charge values represent the mean of three experiments and their standard deviation was indicated.

Light-Driven Propulsion Experiments: The reference spectra of the LED light sources (Colibri 7 with 10× magnification lens, 420 947, Zeiss, Oberkochen, Germany) in the microscope were measured with a calibrated extended range spectrometer (OFX01341, Ocean Optics, FL, USA), using an integration time of 200 ms, a boxcar width of 5, and averaging over five scans. Two measurements were performed with different reflective neutral density filters (Thorlabs, NJ, USA) with an optical density of 3 and 4 to check for consistency.[10] The spot size (3 ± 0.5 mm diameter) of the light beam for the microscope is focused on the surface of the collimator optical fiber of the spectrometer, and the focus is validated with visualization of the field of view on the optical paper. For visible light propulsion and biocompatibility experiments under the microscope, a broad-spectrum low-intensity white LED is illuminated from the top, and lights with various wavelengths (385, 470, 510, 560, and 630 nm) are illuminated through the microscope objective (Figure S8 and Table S1, Supporting Information). The light intensities of the light sources are calculated to be under maximal permissible exposures for ocular safety.[55] The intensity of the microscope light (1 mW cm^{-2} for the control experiments in the dark and 2 mW cm^{-2} for imaging during UV light-based propulsion) was increased to 387 mW cm^{-2} for visible light propulsion. 2D movements of the microswimmers from the microscope videos were tracked with a custom code in MATLAB (R2022a, MathWorks Inc., Natick, MA, USA) (Video S4, Supporting Information). 2D particle motion tracking code can be found in this data repository: https://github.com/erdosty/particletracker2d. For statistical analyses, the Student's *t*-test and one-way ANOVA test were applied (GraphPad Prism 8, San Diego, CA, USA). The p-value was less than 0.01, considered statistically significant for the experimental results.

Biocompatibility Experiments: Human umbilical vein endothelial cells (CRL-1730 [HUVEC], ATCC, Manassas, VA, USA) were grown in dMEM supplemented with 10% (v/v) FBS and 1% (v/v) penicillin/streptomycin (Gibco, Grand Island, NY, USA) at 37 °C in a 5% CO_2, 95% air-humidified atmosphere. Cells were reseeded after growing to confluence into μ-Slide eight-well plates (Ibidi GmbH, Gräfelfing, Germany) at a cell density of 25×10^3 cells $well^{-1}$ and incubated for two days. HUVEC cells were incubated with TAPB-PDA or TpAzo COF microswimmers at varying concentrations (3.1–25 μg mL^{-1}) for cytotoxicity testing. Then, the cell viability was measured using a LIVE/DEAD assay (Thermo Fisher Scientific, Waltham, MA, USA) incorporating calcein-AM (green) and ethidium homodimer-1 (red) dyes. After 24 h of incubation with the COF microswimmers, live-dead cell numbers were calculated from fluorescence microscopy images. Furthermore, cytotoxicity of microswimmers during light actuation (470 nm for TAPB-PDA and 630 nm for TpAzo, 387, and 117 mW cm^{-2}, respectively) was tested by live/dead staining of HUVEC cells right after and 24 h after actuation of COF microswimmers for 30 min.

Drug and ICG Loading and Release Tests: The loading efficiency was measured by centrifuging the DOX (44 583, Sigma-Aldrich, St. Louis, USA) or insulin (I3661, Sigma-Aldrich, St. Louis, USA) loaded microswimmers and comparing the optical density (OD) of the supernatant with the precalibrated OD of DOX or insulin (200 μg mL^{-1}) at 480 nm. Both COF microswimmers (100 μg mL^{-1}) were dispersed with DOX or insulin (200 μg mL^{-1}), and this solution was stirred in the dark for 24 h to allow the drugs to be adsorbed. After 24 h, the suspension was centrifuged, and the supernatant was used for measuring the drug loading. The drug-loaded COF solution was washed three times with water and stored in dPBS at +4 °C for further delivery experiments. For the pH release, the pH of the resulting HCl-diluted PBS solution was checked using a pH meter to confirm the stability of the pH during the release experiments.

NIR-Based Remote Heating of ICG-loaded COF Particles: TpAzo-COF and TAPB-PDA-COF loaded with 50% and 100% ICG were loaded in microtubes and irradiated with a NIR laser (808 nm, 0.6 W cm^{-2}). Thermal images were obtained, and temperature information was recorded with a thermal infrared camera (ETS320, FLIR Systems, OR, USA).

2301126 (11 of 14)

Photoacoustic Imaging Measurements and Analysis: The photoacoustic (PA) signal characterizations were performed inside a Multispectral Optoacoustic Tomography device (MSOT 512-element transducer, iThera Medical, Munich, Germany) system with three scanning steps of 0.2 mm at different wavelengths. The samples with different concentrations were prepared inside a transparent stripe and embedded in an agar phantom (1.5 g/100 mL agar-DI water). The same preparation was done for the control sample. The agar phantom was placed at the center of the transducer arrays. The measurements were then taken for a range of wavelengths (660–980 nm), and each image was repeated three times for each laser pulse and then averaged. A circular region of interest (ROI) was chosen for calculating the PA signal at each wavelength. Finally, the diagrams were plotted against the control sample for all concentrations.

For PA imaging of light-induced motion of nanoparticles, a handheld 3D photoacoustic probe (256-element transducer, iThera Medical, Munich, Germany) was used for real-time tracking. The laser wavelength was set at 800 nm, and the image sequences were taken at 10 frames s^{-1}. Then, a volumetric image of $20 \times 20 \times 20$ mm^3 was constructed from three orthogonal imaging planes. The real-time change in the signal intensity at the light actuation spot indicated the movement of the nanoparticles.

Optical Coherence Tomography: The fresh porcine eyes were purchased from Ulmer Fleisch food factory, Ulm, Germany. Within 6 h after the euthanasia of the animals, a set of enucleated eyes stabilized to the holder, and COFs were injected with a 30G syringe in the anterior chambers of the porcine eyes before OCT imaging. The porcine eyes were illuminated with collimated directional light (470 and 630 nm) through the cornea. Besides that, aqueous humor was removed from another set of fresh porcine eyes with the help of a 30G trocar and cannula. For vitreous collection, a classical vitrectomy procedure is followed.[65] The intraocular fluids with COFs were injected into a cylindrical tubing and observed via OCT (TEL320C1—Spectral Domain OCT System, Thorlabs, NJ, USA). Similar to ex vivo experiments, one side of the cylindrical tubing was illuminated with a collimated directional light (470 and 630 nm). The motion inside the eye was recorded with an image speed at a medium sensitivity (76 kHz). The refractive index was set to 1.00, and the Hann filter was used for the apodization window. The A-scan averaging was set to 1, and the B-scan averaging to 1 with a pixel size of 6.5 µm. For both photoacoustic and optical coherence tomography imaging experiments, a calibrated Thorlabs S425C/PM100D optical power meter was used to measure the light intensity on the sample surface, and a collimator lens tube was used to illuminate on the spot size. The illumination was adjusted to corresponding peak light intensities in the light propulsion experiments. The average pixel intensity for the light and dark sides of the tubings was normalized and measured with ImageJ software (NIH, MD, USA). For statistical analysis, the Student's *t*-test was applied (GraphPad Prism 8, San Diego, CA, USA). The *p*-value < 0.01, considered statistically significant for the experimental results.

Supporting Information

Supporting Information is available from the Wiley Online Library or from the author.

Conflict of Interest

The authors declare no conflict of interest.

Author Contributions

V.S. and E.Y. contributed equally to this work. F.P., V.S., B.V.L., and M.S. conceived and designed the project. F.P., V.S., and E.Y. wrote the manuscript, with input and corrections from all authors. A.R. and L.Y synthesized and characterized the materials. V.S. and X.L. performed the light propulsion experiments and analyzed the data. E.Y. performed and analyzed in vitro biocompatibility tests. X.L. and M.B.A. performed and analyzed drug loading experiments. B. A. performed and analyzed NIR hyperthermia experiments. A.A., E.Y., and P.W. performed and analyzed the photoacoustic imaging. E.Y. isolated porcine intraocular fluids and performed optical coherence tomography. M.S., F.P., and B.V.L. supervised the research. All authors contributed to the discussion of the data and overall results.

Data Availability Statement

The data that support the findings of this study are available from the corresponding author upon reasonable request.

[1] a) P. E. Dupont, B. J. Nelson, M. Goldfarb, B. Hannaford, A. Menciassi, M. K. O'Malley, N. Simaan, P. Valdastri, G. Z. Yang, *Sci. Robot.* **2021**, *6*, eabi8017; b) P. Erkoc, I. C. Yasa, H. Ceylan, O. Yasa, Y. Alapan, M. Sitti, *Adv. Ther.* **2019**, *2*, 1800064; c) M. Sitti, *Mobile Microrobotics*, MIT Press, Cambridge, MA, USA **2017**.

[2] a) J. Mujtaba, J. Liu, K. K. Dey, T. Li, R. Chakraborty, K. Xu, D. Makarov, R. A. Barmin, D. A. Gorin, V. P. Tolstoy, G. Huang, A. A. Solovev, Y. Mei, *Adv. Mater.* **2021**, *33*, 2007465; b) F. Soto, J. Wang, R. Ahmed, U. Demirci, *Adv. Sci.* **2020**, *7*, 2002203.

[3] a) M. Sitti, D. S. Wiersma, *Adv. Mater.* **2020**, *32*, 1906766; b) Z. Wu, Y. Chen, D. Mukasa, O. S. Pak, W. Gao, *Chem. Soc. Rev.* **2020**, *49*, 8088.

[4] S. K. Srivastava, G. Clergeaud, T. L. Andresen, A. Boisen, *Adv. Drug Delivery Rev.* **2019**, *138*, 41.

[5] V. Sridhar, F. Podjaski, Y. Alapan, J. Kroger, L. Grunenberg, V. Kishore, B. V. Lotsch, M. Sitti, *Sci. Rob.* **2022**, *7*, eabm1421.

[6] a) L. Kong, C. C. Mayorga-Martinez, J. Guan, M. Pumera, *Small* **2020**, *16*, 1903179; b) J. Wang, Z. Xiong, J. Tang, *Adv. Intell. Syst.* **2021**, *3*, 2000170; c) A. Gulzar, E. Yıldız, H. N. Kaleli, M. A. Nazeer, N. Zibandeh, A. N. Malik, A. Y. Taş, I. Lazoğlu, A. Şahin, S. Kizilel, *Acta Biomater.* **2022**, *147*, 198.

[7] N. M. Idris, M. K. Gnanasammandhan, J. Zhang, P. C. Ho, R. Mahendran, Y. Zhang, *Nat. Med.* **2012**, *18*, 1580.

[8] a) C. K. Schmidt, M. Medina-Sanchez, R. J. Edmondson, O. G. Schmidt, *Nat. Commun.* **2020**, *11*, 5618; b) A. M. Vargason, A. C. Anselmo, S. Mitragotri, *Nat. Biomed. Eng.* **2021**, *5*, 951; c) B. Wang, K. Kostarelos, B. J. Nelson, L. Zhang, *Adv. Mater.* **2021**, *33*, 2002047.

[9] a) J. Li, X. Yu, M. Xu, W. Liu, E. Sandraz, H. Lan, J. Wang, S. M. Cohen, *J. Am. Chem. Soc.* **2017**, *139*, 611; b) G. Lin, J. J. Richardson,

H. Ahmed, Q. A. Besford, A. J. Christofferson, S. Beyer, Z. Lin, A. R. Rezk, M. Savioli, J. Zhou, C. F. McConville, C. Cortez-Jugo, L. Y. Yeo, F. Caruso, *Adv. Mater.* **2021**, *33*, 2006177; c) K. Vikrant, K.-H. Kim, *Catal. Sci. Technol.* **2021**, *11*, 6592.

[10] V. Sridhar, F. Podjaski, J. Kroger, A. Jimenez-Solano, B. W. Park, B. V. Lotsch, M. Sitti, *Proc. Natl. Acad. Sci. USA* **2020**, *117*, 24748.

[11] F. Haase, B. V. Lotsch, *Chem. Soc. Rev.* **2020**, *49*, 8469.

[12] a) M. S. Kim, H. T. Lee, S. H. Ahn, *Adv. Mater. Technol.* **2019**, *4*, 1900583; b) F. Ullrich, C. Bergeles, J. Pokki, O. Ergeneman, S. Erni, G. Chatzipirpiridis, S. Pane, C. Framme, B. J. Nelson, *Invest. Ophthalmol. Visual Sci.* **2013**, *54*, 2853; c) Z. Wu, J. Troll, H. H. Jeong, Q. Wei, M. Stang, F. Ziemssen, Z. Wang, M. Dong, S. Schnichels, T. Qiu, P. Fischer, *Sci. Adv.* **2018**, *4*, eaat4388.

[13] a) V. S. Vyas, B. V. Lotsch, *Nature* **2015**, *521*, 41; b) W. Zhao, L. Xia, X. Liu, *CrystEngComm* **2018**, *20*, 1613.

[14] a) J. M. McCracken, B. R. Donovan, T. J. White, *Adv. Mater.* **2020**, *32*, 1906564; b) H. Wang, H. Wang, Z. Wang, L. Tang, G. Zeng, P. Xu, M. Chen, T. Xiong, C. Zhou, X. Li, D. Huang, Y. Zhu, Z. Wang, J. Tang, *Chem. Soc. Rev.* **2020**, *49*, 4135.

[15] D. Zhou, R. Zhuang, X. Chang, L. Li, *Research* **2020**, *2020*, 6821595.

[16] B. Lee, M. Litt, G. Buchsbaum, *Biorheology* **1992**, *29*, 521.

[17] R. L. Li, N. C. Flanders, A. M. Evans, W. Ji, I. Castano, L. X. Chen, N. C. Gianneschi, W. R. Dichtel, *Chem. Sci.* **2019**, *10*, 3796.

[18] A. P. Cote, H. M. El-Kaderi, H. Furukawa, J. R. Hunt, O. M. Yaghi, *J. Am. Chem. Soc.* **2007**, *129*, 12914.

[19] M. S. Lohse, T. Bein, *Adv. Funct. Mater.* **2018**, *28*, 1705553.

[20] Z. Wu, Y. Zhang, N. Ai, H. Chen, W. Ge, Q. Xu, *Adv. Intell. Syst.* **2022**, *4*, 2100266.

[21] a) M. Wei, C. Zhou, J. Tang, W. Wang, *ACS Appl. Mater. Interfaces* **2018**, *10*, 2249; b) X. Zhan, J. Wang, Z. Xiong, X. Zhang, Y. Zhou, J. Zheng, J. Chen, S. P. Feng, J. Tang, *Nat. Commun.* **2019**, *10*, 3921.

[22] Z. Liang, R. Shen, Y. H. Ng, Y. Fu, T. Ma, P. Zhang, Y. Li, X. Li, *Chem. Catal.* **2022**, *2*, 2157.

[23] L. M. Peter, *Photocatalysis: Fundamentals and Perspectives*, (Eds: J. Schneider, D. Bahnemann, J. Ye, G. Li Puma, D. D. Dionysiou), The Royal Society of Chemistry, **2016**.

[24] a) K. Xiao, L. Chen, R. Chen, T. Heil, S. D. C. Lemus, F. Fan, L. Wen, L. Jiang, M. Antonietti, *Nat. Commun.* **2019**, *10*, 74; b) F. Xu, M. Wei, X. Zhang, Y. Wang, *ACS Appl. Mater. Interfaces* **2019**, *11*, 45246.

[25] A. Gouder, A. Jimenez-Solano, N. M. Vargas-Barbosa, F. Podjaski, B. V. Lotsch, *Mater. Horiz.* **2022**, *9*, 1866.

[26] J. Wang, Z. Xiong, X. Zhan, B. Dai, J. Zheng, J. Liu, J. Tang, *Adv. Mater.* **2017**, *29*, 1701451.

[27] a) J. Kröger, A. Jiménez-Solano, G. Savasci, V. W. h. Lau, V. Duppel, I. Moudrakovski, K. Küster, T. Scholz, A. Gouder, M. L. Schreiber, F. Podjaski, C. Ochsenfeld, B. V. Lotsch, *Adv. Funct. Mater.* **2021**, *31*, 2102468; b) J. Kröger, F. Podjaski, G. Savasci, I. Moudrakovski, A. Jimenez-Solano, M. W. Terban, S. Bette, V. Duppel, M. Joos, A. Senocrate, R. Dinnebier, C. Ochsenfeld, B. V. Lotsch, *Adv. Mater.* **2022**, *34*, 2107061.

[28] a) C. Chen, F. Mou, L. Xu, S. Wang, J. Guan, Z. Feng, Q. Wang, L. Kong, W. Li, J. Wang, Q. Zhang, *Adv. Mater.* **2017**, *29*, 1603374; b) B. Dai, J. Wang, Z. Xiong, X. Zhan, W. Dai, C. C. Li, S. P. Feng, J. Tang, *Nat. Nanotechnol.* **2016**, *11*, 1087.

[29] W. E. Uspal, *J. Chem. Phys.* **2019**, *150*, 114903.

[30] M. You, C. Chen, L. Xu, F. Mou, J. Guan, *Acc. Chem. Res.* **2018**, *51*, 3006.

[31] L.-J. Chen, S. Ito, H. Kai, K. Nagamine, N. Nagai, M. Nishizawa, T. Abe, H. Kaji, *Sci. Rep.* **2017**, *7*, 3538.

[32] R. H. Soon, Z. Ren, W. Hu, U. Bozuyuk, E. Yildiz, M. Li, M. Sitti, *Proc. Natl. Acad. Sci. USA* **2022**, *119*, e2207767119.

[33] Y. Zhou, S. Liu, C. Hu, L. Cai, M. Pang, *J. Mater. Chem. B* **2020**, *8*, 5451.

[34] M. Mehta, *Biopharmaceutics Classification System (BCS): Development, Implementation, and Growth*, Wiley, Hoboken, NJ, USA **2017**.

[35] U. B. Kompella, A. C. Amrite, R. Pacha Ravi, S. A. Durazo, *Prog. Retinal Eye Res* **2013**, *36*, 172.

[36] H. Dimaras, K. Kimani, E. A. Dimba, P. Gronsdahl, A. White, H. S. Chan, B. L. Gallie, *Lancet* **2012**, *379*, 1436.

[37] P. Bilalis, L.-A. Tziveleka, S. Varlas, H. Iatrou, *Polym. Chem.* **2016**, *7*, 1475.

[38] W. A. Lestari, S. Wahyuningsih, S. Gomez-Ruiz, F. R. Wibowo, *J. Phys.: Conf. Ser.* **2022**, *2190*, 012032.

[39] M. Ibrahim, W. H. Abuwatfa, N. S. Awad, R. Sabouni, G. A. Husseini, *Pharmaceutics* **2022**, *14*, 254.

[40] a) C. R. Justus, L. Dong, L. V. Yang, *Front. Physiol.* **2013**, *4*, 354; b) Q. Lin, J. M. Pilewski, Y. P. Di, *Front. Microbiol.* **2021**, *12*, 747834.

[41] a) J. Broichhagen, M. Schonberger, S. C. Cork, J. A. Frank, P. Marchetti, M. Bugliani, A. M. Shapiro, S. Trapp, G. A. Rutter, D. J. Hodson, D. Trauner, *Nat. Commun.* **2014**, *5*, 5116; b) C. E. Reiter, T. W. Gardner, *Prog. Retinal Eye Res.* **2003**, *22*, 545.

[42] L. A. Yannuzzi, *Am. J. Ophthalmol.* **2011**, *151*, 745.

[43] K. Gowsalya, V. Yasothamani, R. Vivek, *Nanoscale Adv.* **2021**, *3*, 3332.

[44] a) L. Li, Z. Zeng, Z. Chen, R. Gao, L. Pan, J. Deng, X. Ye, J. Zhang, S. Zhang, C. Mei, J. Yu, Y. Feng, Q. Wang, A. Y. Yu, M. Yang, J. Huang, *ACS Nano* **2020**, *14*, 15403; b) D. Liu, Q. Wu, W. Chen, K. Chen, H. Lin, F. Liu, X. Xie, H. J. Chen, W. Chen, *Small* **2022**, *18*, 2201098.

[45] A. Aziz, S. Pane, V. Iacovacci, N. Koukourakis, J. Czarske, A. Menciassi, M. Medina-Sanchez, O. G. Schmidt, *ACS Nano* **2020**, *14*, 10865.

[46] a) C. Kesim, S. N. Bektas, Z. Kulali, E. Yildiz, M. G. Ersoz, A. Sahin, C. Gunduz-Demir, M. Hasanreisoglu, *Retina* **2022**, *42*, 1780; b) W. Drexler, U. Morgner, R. K. Ghanta, F. X. Kartner, J. S. Schuman, J. G. Fujimoto, *Nat. Med.* **2001**, *7*, 502.

[47] a) S. Jeon, H. B. Song, J. Kim, B. J. Lee, R. Managuli, J. H. Kim, J. H. Kim, C. Kim, *Sci. Rep.* **2017**, *7*, 4318; b) Y. H. Yucel, K. Cardinell, S. Khattak, X. Zhou, M. Lapinski, F. Cheng, N. Gupta, *Invest. Ophthalmol. Visual Sci.* **2018**, *59*, 2699.

[48] A. Aziz, J. Holthof, S. Meyer, O. G. Schmidt, M. Medina-Sanchez, *Adv. Healthcare Mater.* **2021**, *10*, 2101077.

[49] E. M. del Amo, A.-K. Rimpelä, E. Heikkinen, O. K. Kari, E. Ramsay, T. Lajunen, M. Schmitt, L. Pelkonen, M. Bhattacharya, D. Richardson, A. Subrizi, T. Turunen, M. Reinisalo, J. Itkonen, E. Toropainen, M. Casteleijn, H. Kidron, M. Antopolsky, K.-S. Vellonen, M. Ruponen, A. Urtti, *Prog. Retinal Eye Res.* **2017**, *57*, 134.

[50] a) K. Fujiwara, M. Yasuda, T. Ninomiya, J. Hata, S. Hashimoto, T. Yoshitomi, Y. Kiyohara, T. Ishibashi, *Invest. Ophthalmol. Visual Sci.* **2015**, *56*, 7983; b) G. Velez, P. Yuan, C. Sung, G. Tansey, G. F. Reed, C. C. Chan, R. B. Nussenblatt, M. R. Robinson, *Arch. Ophthalmol.* **2001**, *119*, 1518.

[51] a) Z. Mu, Y. Zhu, B. Li, A. Dong, B. Wang, X. Feng, *J. Am. Chem. Soc.* **2022**, *144*, 5145; b) H. Salemi, M. Debruyne, V. Van Speybroeck, P. Van Der Voort, M. D'Hooghe, C. V. Stevens, *J. Mater. Chem. A* **2022**, *10*, 20707.

[52] H. Li, J. Ding, X. Guan, F. Chen, C. Li, L. Zhu, M. Xue, D. Yuan, V. Valtchev, Y. Yan, S. Qiu, Q. Fang, *J. Am. Chem. Soc.* **2020**, *142*, 13334.

[53] a) S. Crespi, N. A. Simeth, B. König, *Nat. Rev. Chem.* **2019**, *3*, 133; b) J. Zhao, J. Ren, G. Zhang, Z. Zhao, S. Liu, W. Zhang, L. Chen, *Chemistry* **2021**, *27*, 10781.

[54] Y. Chen, M. Li, Q. Tang, Y. Cheng, A. Miao, L. Cheng, S. Zhu, T. Luo, G. Liu, L. Zhang, F. Niu, L. Zhao, J. Chen, R. Yang, *Adv. Intell. Syst.* **2023**, *5*, 2200311.

[55] F. C. Delori, R. H. Webb, D. H. Sliney, *J. Opt. Soc. Am. A: Opt. Image Sci. Vis.* **2007**, *24*, 1250.

[56] M. Yang, A. Wysocki, M. Ripoll, *Soft Matter* **2014**, *10*, 6208.

[57] a) F. Zhou, Y. Fang, C. Deng, Q. Zhang, M. Wu, H. H. Shen, Y. Tang, Y. Wang, *Nanomaterials* **2022**, *12*, 3055; b) C. Wang, H. Liu, S. Liu, Z. Wang, J. Zhang, *Front. Chem.* **2020**, *8*, 488.

[58] V. S. Vyas, F. Haase, L. Stegbauer, G. Savasci, F. Podjaski, C. Ochsenfeld, B. V. Lotsch, *Nat. Commun.* **2015**, *6*, 8508.

[59] M. Li, Y. Peng, F. Yan, C. Li, Y. He, Y. Lou, D. Ma, Y. Li, Z. Shi, S. Feng, *New J. Chem.* **2021**, *45*, 3343.

[60] J.-Y. Zeng, X.-S. Wang, B.-R. Xie, M.-J. Li, X.-Z. Zhang, *Angew. Chem., Int. Ed.* **2020**, *59*, 10087.

[61] F. Benyettou, N. Kaddour, T. Prakasam, G. Das, S. K. Sharma, S. A. Thomas, F. Bekhti-Sari, J. Whelan, M. A. Alkhalifah, M. Khair, H. Traboulsi, R. Pasricha, R. Jagannathan, N. Mokhtari-Soulimane, F. Gandara, A. Trabolsi, *Chem. Sci.* **2021**, *12*, 6037.

[62] T. C. Pham, V. N. Nguyen, Y. Choi, S. Lee, J. Yoon, *Chem. Rev.* **2021**, *121*, 13454.

[63] S. Chandra, T. Kundu, S. Kandambeth, R. Babarao, Y. Marathe, S. M. Kunjir, R. Banerjee, *J. Am. Chem. Soc.* **2014**, *136*, 6570.

[64] Z. Chen, H. N. Dinh, E. Miller, *Photoelectrochemical Water Splitting*, Vol. *344*, Springer, Berlin, Germany **2013**.

[65] S. Mohamed, C. Claes, C. W. Tsang, *J. Ophthalmol.* **2017**, *2017*, 6285869.

2301126 (14 of 14)